Geophysical Journal International

Geophys. J. Int. (2022) **230,** 528–541
Advance Access publication 2022 February 9
GJI Seismology

https://doi.org/10.1093/gji/ggac059

Fast rupture of the 2009 M_w 6.9 Canal de Ballenas earthquake in the Gulf of California dynamically triggers seismicity in California

Wenyuan Fan [1], Ryo Okuwaki [2], Andrew J. Barbour [3], Yihe Huang,[4] Guoqing Lin[5] and Elizabeth S. Cochran [6]

[1] *Scripps Institution of Oceanography, UC San Diego, La Jolla, CA,* 92093*, USA . E-mail: wenyuanfan@ucsd.edu*
[2] *Mountain Science Center, Faculty of Life and Environmental Sciences, University of Tsukuba, Tsukuba, Ibaraki,* 305-8572*, Japan*
[3] *U.S. Geological Survey, Earthquake Science Center, Moffett Field, CA,* 94035*, USA*
[4] *Department of Earth and Environmental Sciences, University of Michigan, Ann Arbor, MI,* 48109*, USA*
[5] *Rosenstiel School of Marine and Atmospheric Science, University of Miami, Miami, FL,* 33149*, USA*
[6] *U.S. Geological Survey, Earthquake Science Center, Pasadena, CA,* 91106*, USA*

Accepted 2022 February 7. Received 2022 January 20; in original form 2021 September 9

SUMMARY

In the Gulf of California, Mexico, the relative motion across the North America–Pacific boundary is accommodated by a series of marine transform faults and spreading centres. About 40 $M > 6$ earthquakes have occurred in the region since 1960. On 2009 August 3, an M_w 6.9 earthquake occurred near Canal de Ballenas in the region. The earthquake was a strike-slip event with a shallow hypocentre that is likely close to the seafloor. In contrast to an adjacent $M7$ earthquake, this earthquake triggered a ground-motion-based earthquake early warning algorithm being tested in southern California (∼600 km away). This observation suggests that the abnormally large ground motions and dynamic strains observed for this earthquake relate to its rupture properties. To investigate this possibility, we image the rupture process and resolve the slip distribution of the event using a *P*-wave backprojection approach and a teleseismic, finite-fault inversion method. Results from these two independent analyses indicate a relatively simple, unilateral rupture propagation directed along-strike in the northward direction. However, the average rupture speed is estimated around 4 km s^{-1}, suggesting a possible supershear rupture. The supershear speed is also supported by a Rayleigh wave Mach cone analysis, although uncertainties in local velocity structure preclude a definitive conclusion. The Canal de Ballenas earthquake dynamically triggered seismicity at multiple sites in California, with triggering response characteristics varying from location-to-location. For instance, some of the triggered earthquakes in California occurred up to 24 hr later, suggesting that nonlinear triggering mechanisms likely have modulated their occurrence.

Key words: Earthquake dynamics; Earthquake ground motions; Earthquake interaction, forecasting, and prediction; Earthquake source observations.

1 INTRODUCTION

The transtensional, plate boundary fault system in the Gulf of California (GoC), Mexico, comprises right-lateral transform faults connecting the San Andreas fault and the East Pacific Rise, extending over 1300 km (Atwater & Stock 1998; Axen *et al.* 2000). The fault system accommodates about 90 per cent of the North America–Pacific relative plate motion, which is segmented with short extensional basins and spreading ridges transitioning from continental extension to seafloor spreading (DeMets *et al.* 1990, 1994; DeMets & Dixon 1999; Plattner *et al.* 2007, 2009). In southern GoC, the transform fault-spreading centre connects with the East Pacific Rise and earthquakes in the region have relatively simple source attributes (Goff *et al.* 1987; McCrory *et al.* 2009; Sumy *et al.* 2013). In contrast, the northern GoC has a more complex fault system. For example, the lower Delfin basin (Fig. 1), the largest active basin in the northern GoC, is rich in both magmatic activity and faulting (Persaud *et al.* 2003; Castro *et al.* 2011a).

The Canal de Ballenas fault zone connects the lower Delfin basin to the Guaymas basin further in the south (Lonsdale 1985; Plattner *et al.* 2015); it represents the northern part of the Guaymas fault system, which extends over 350 km (Lonsdale 1985). The Canal de Ballenas fault zone is about 93 km long and has a width of 10–20 km,

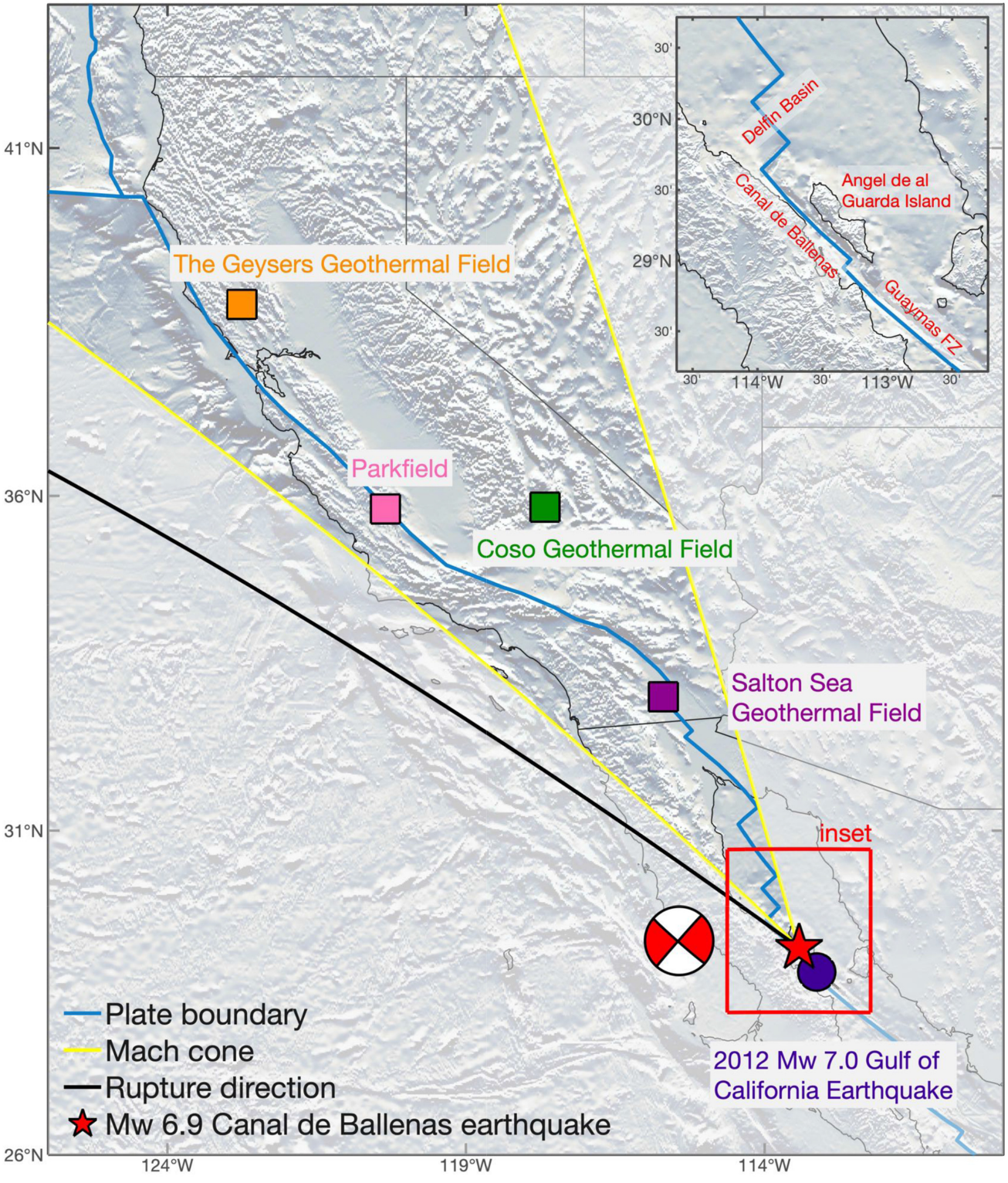

Figure 1. The 2009 *M*6.9 Canal de Ballenas earthquake and the Salton Sea Geothermal Field (latitude/longitude, 33.02°/−115.70°), Coso Geothermal Field (35.83°/−117.68°), Parkfield (35.80°/−120.35°) and The Geysers Geothermal Field (38.78°/−122.75°). Seismicity rate changes up to 24 hr after the Canal de Ballenas earthquake have been investigated at these four sites. For reference, the location of the nearby 2012 *M*7.0 is shown. Inset: geologic features near the Canal de Ballenas earthquake.

occupying the Ballenas Channel and separating the Baja California peninsula and Angel de la Guarda Island (Castro *et al.* 2011a,b). The Ballenas transform fault changes its strike about 10° from the continental Cerro Prieto transform fault, suggesting a transition between the oceanic and the continental transform systems (Goff *et al.* 1987; Plattner *et al.* 2007). Deformation in the channel is highly localized, forming clear, linear fault traces (Lonsdale 1985; Plattner *et al.* 2015).

On 2009 August 3, an M_w 6.9 earthquake ruptured this fault, showing a consistent strike-slip focal mechanism (Castro *et al.* 2011b; Ekström *et al.* 2012). The earthquake is one of the largest earthquakes in the region in modern time, and may have ruptured to the seafloor with a shallow hypocentre (Castro *et al.* 2011b; Plattner *et al.* 2015). The M_w 6.9 earthquake caused an earthquake early warning algorithm being tested in southern California to issue a false detection during retrospective analyses (Cochran *et al.* 2019). Intriguingly, the 2012 April 12 M_w 7.0 Gulf of California earthquake, which is only 51 km away from the 2009 M_w 6.9 earthquake, did not produce similar ground motions in southern California (Fig. 1). The differences suggest that the rupture propagation of the 2009 Canal de Ballenas earthquake is responsible for the abnormally large ground motions. Understanding the earthquake rupture process would help interpreting the local faulting process and the regional seismotectonics.

Here, we image the earthquake rupture propagation with a backprojection method and obtain a kinematic slip distribution with a teleseismic finite-fault inversion method. Both models suggest the earthquake ruptured along strike, towards the north, but also that the rupture speed may have exceeded local shear wave speed—a supershear rupture. We further investigate the associated seismicity rate changes seen in California with three different earthquake catalogues. We find the 2009 M_w 6.9 earthquake dynamically triggered earthquakes at multiple sites in California, including three geothermal fields and the Parkfield segment of the San Andreas fault. This complex set of slip events highlights the triggering and interaction processes across global-scale fault systems.

2 DATA SETS AND METHODS

2.1 Backprojection

We analyse the rupture propagation of the 2009 M_w 6.9 Canal de Ballenas earthquake following a standard time-domain backprojection method (Fig. 2; Ishii *et al.* 2005; Fan & Shearer 2015). We first download *P*-wave velocity records of the event from stations within 30° to 90° epicentral distance (see Data Availability). We apply a 0.05–0.25 Hz second-order Butterworth filter. Records with signal-to-noise ratios (SNRs) less than 5 are removed. The SNR is defined as the root-mean-square (RMS) amplitude ratio from time windows 10 s before and 10 s after the theoretical *P*-wave arrival obtained from AK135 (Kennett *et al.* 1995). Stations that are close to the nodal plane directions are also discarded. We then visually examine the records to only keep traces with clear *P*-wave onsets. After the initial quality control steps, the traces are aligned using multichannel cross-correlation with a time window from -2 to 8 s relative to the theoretical *P* arrivals. Polarity flips are allowed during cross-correlation to accommodate the varying radiation patterns at different azimuths. In summary, 82 stations are used to image the rupture evolution of the Canal de Ballenas earthquake (inset, Fig. 2a).

Backprojection is effective at resolving earthquake radiation and detecting hidden aftershocks of large earthquakes because the method does not assume a fault geometry or a rupture velocity (Fan & Shearer 2016; Nissen *et al.* 2016). The method has been successfully implemented to study spatiotemporal evolution of complex earthquakes, including multifault rupture events and supershear earthquakes (Meng *et al.* 2012; Yagi & Okuwaki 2015; Wang *et al.* 2016; Okuwaki *et al.* 2020). For the backprojection procedure, we set a grid of potential sources around the hypocentre (Castro *et al.* 2011b) with a 10-km horizontal grid spacing fixed at the hypocentral depths. The potential source grids cover a 600 km × 600 km area for the earthquake with its epicentre at the centre of the grids. Backprojection is then performed with the *N*th root stacking method (Rost & Thomas 2002; Xu *et al.* 2009) with $N = 4$. The *N*th root method can improve spatial resolution of backprojection images, albeit at the cost of losing absolute amplitude information (Rost & Thomas 2002; Xu *et al.* 2009). Seismic records are self-normalized and inversely scaled by the number of contributing stations within 5°, which helps to balance differences in azimuthal and spatial coverage of the stations. To evaluate the spatiotemporal migration, we compute backprojection snapshots with 8-s stacking windows; these snapshots are normalized by the maximum power within each window and are shown as contours with coherence above 85 per cent of the maximum normalized energy (Fig. 2).

To assess the robustness of the backprojection images, we performed three different tests to evaluate the results. First, we calculate the theoretical resolving power to estimate the best possible resolution for a given network in the frequency bands of interest (Supporting Information Figs S1a and b). For this test, we randomly assign a recorded *P* wave train to all the stations, then backproject these traces following the same procedure that is used to image the Canal de Ballenas earthquake. From this test, the array resolution is about 20 km for the earthquake at 0.05–0.25 Hz frequency band (Supporting Information Figs S1a and b). Second, we image a few smaller earthquakes in the same region. This test can help to assess potential biases introduced by the complexities of the wavefield and the path effects (Supporting Information Figs S1c–f). The obtained image represents the lower resolution limit. This is because smaller magnitude events often have noisy data. We performed backprojection on two nearby earthquakes within 5° at the same frequency band with similar array configurations (Supporting Information Figs S1c–f). The images of these earthquakes have spatial extents around 20 km on average, and are free of obvious artefacts, including possible artefacts from water reverberations (Supporting Information Figs S1c–f). The spatial extents are comparable to the snapshot energy bursts in Fig. 2(b), confirming the rupture episodes of the Canal de Ballenas earthquake. Aftershocks immediately adjacent to the 2009 M_w 6.9 Canal de Ballenas earthquake have low SNRs, limiting their use for assessing the near-source 3-D velocity effects on the images. However, previous studies show that such effects may cause location uncertainties less than 25 km (Fan & Shearer 2017). Finally, we use jackknife resampling to quantitatively evaluate the robustness of the resolved radiation episodes (Efron & Tibshirani 1994; Fan & Shearer 2016). For the three time windows, the distances from the epicentre to the peak loci have spatial uncertainties of one standard deviation as 0, 6 and 29 km (inset, Fig. 2b). The standard deviation of the first time window is 0 because of the initial alignment. We do not stack or post-process the backprojection images to avoid subjective choices. All these tests indicate that our backprojection results are well resolved.

2.2 Finite-fault inversion

To resolve the slip development, we perform a finite-fault slip inversion of the 2009 M_w 6.9 earthquake using newly developed potency–density tensor approach following Shimizu *et al.* (2020; Figs 3 and 4). The method is designed to produce slip distributions that account for uncertainties in the Green's function and the fault geometry, which often represent major modelling errors in finite-fault inversion (Yagi & Fukahata 2011; Duputel *et al.* 2014; Ragon

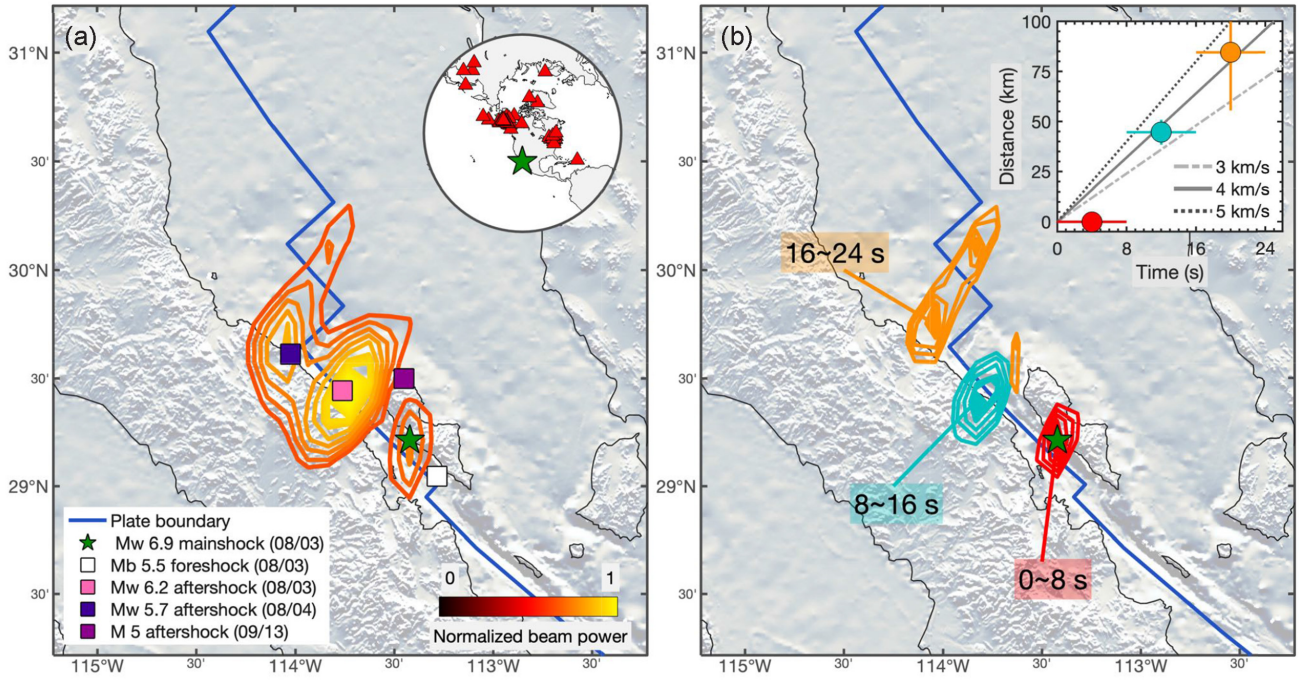

Figure 2. Backprojection results of the 2009 *M*6.9 Canal de Ballenas earthquake and the associated surface wave observations. (a) Integrated backprojection image of the earthquake (60 per cent normalized energy contours). Inset: stations used for backprojection. (b) Backprojection snapshots of the earthquake. Inset: cumulative distance as a function of time. The location uncertainties are obtained from a jackknife analysis.

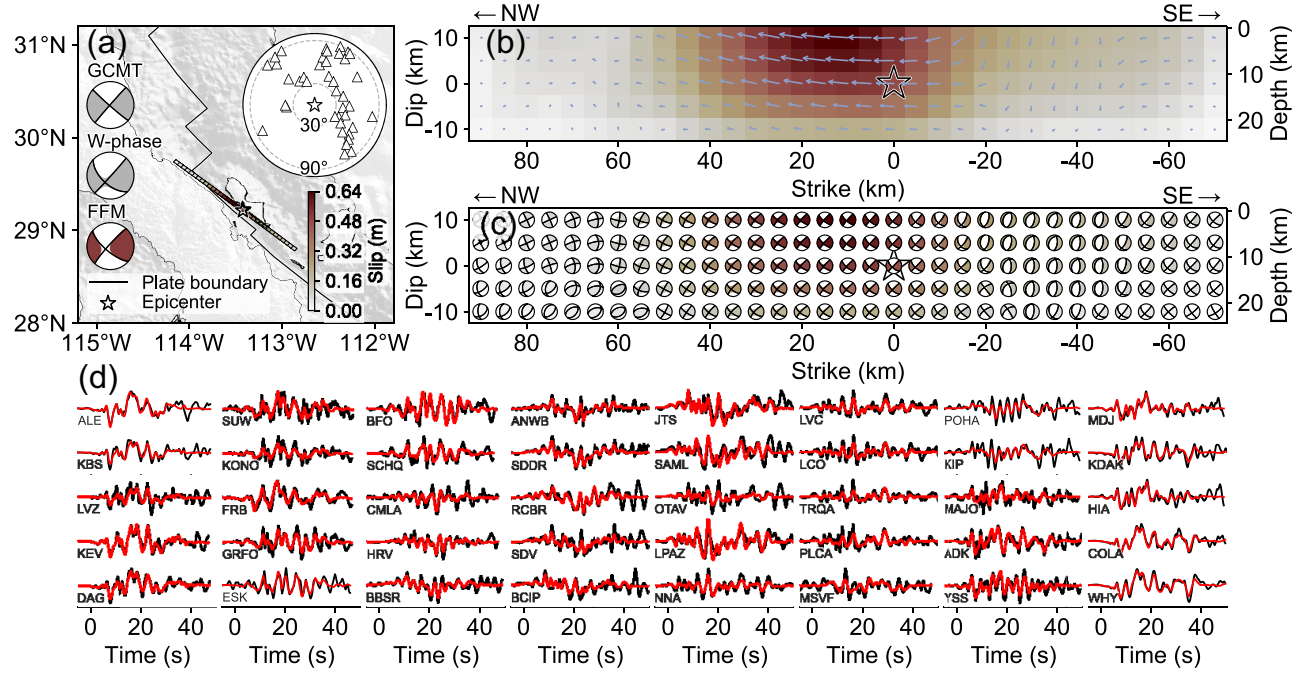

Figure 3. Finite-fault inversion results of the 2009 *M*6.9 Canal de Ballenas earthquake. (a) Map view of the slip distribution. The colour of subfault cell shows the slip amplitude. The largest slip cell along depth is shown for each column of the model fault. Inset: stations used for finite-fault inversion. The beach balls are the centroid moment tensor solutions from the Global Centroid Moment Tensor (GCMT) catalogue (Ekström *et al.* 2012), the USGS W-phase moment tensor solution (Duputel *et al.* 2012; U.S. Geological Survey Earthquake Hazards Program 2017), and the FFM of this study. The background bathymetry/topography is from the GEBCO 2019 Grid (GEBCO Bathymetric Compilation Group 2019). (b) The cross-section of the static slip distribution with the same colourmap in (a). The star shows the hypocentre. The arrow shows the rake angle. Note that the abscissa is inverted. (c) The cross-section of the moment-tensor distribution extracted from the resultant potency–density tensors. Only the double-couple component is shown. All the beach balls of the moment-tensor solution are represented as a lower-hemisphere stereographic projection (far-side focal sphere). These are not cross-section of focal-mechanisms. (d) The waveform fitting between the observed (black) and the synthetic (red) waveforms. The station code is shown in each panel.

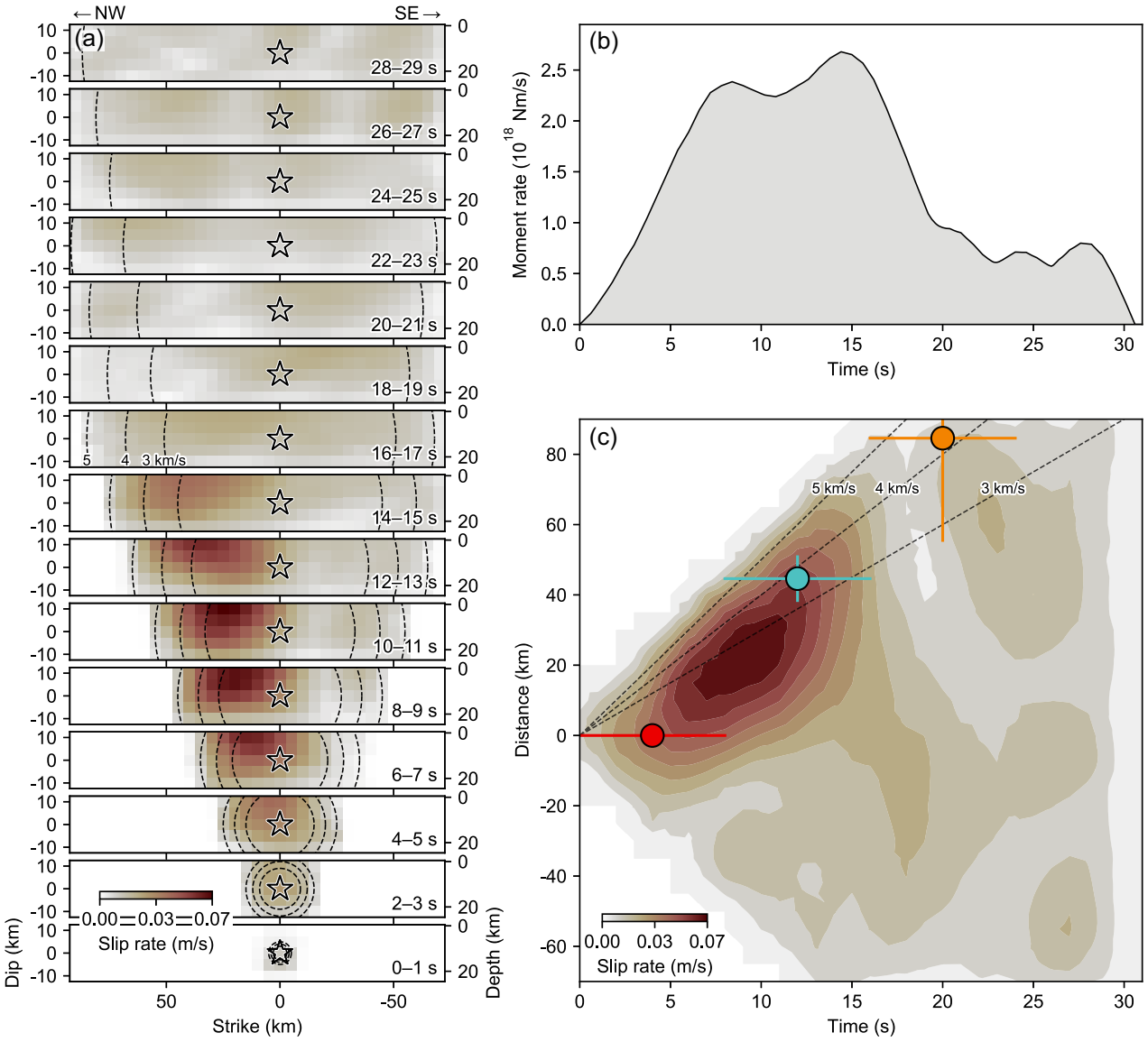

Figure 4. Slip evolution of the 2009 *M*6.9 Canal de Ballenas earthquake. (a) Snapshots of the cross-section of the slip-rate distribution. The star shows the hypocentre. The dashed circles are the reference rupture speeds circularly expanding from the hypocentre. The time window for each snapshot is shown at bottom-right for each panel. (b) The moment-rate function. (c) Temporal evolution of the slip rate, projected along the model-fault strike (310°). The dashed lines are the reference rupture speeds. The backprojection result (Fig. 2b) is overlain.

et al. 2018; Shimizu *et al.* 2020). Instead of fixing the fault-normal and slip directions on a fault, as conventional finite-fault inversion methods do, in our method the slip of each subfault is flexibly represented by a linear combination of five basis double-couple components of the potency–density tensors (Kikuchi & Kanamori 1991; Ampuero & Dahlen 2005), which are independent of the modelled fault geometry. In other words, our method solves for the mechanisms of distributed potential sources on the modelled fault, allowing for any type of faulting mechanisms required by the data, and limiting the number of assumptions needed about fault geometry. The procedure allows resolving complex earthquake rupture processes. The finite-fault model (FFM) space is designed based on prior observations (e.g. backprojection and aftershock distribution).

For the finite-fault inversion, we use vertical components of teleseismic *P* waveforms from 40 stations (Fig. 3a), which are manually selected to achieve a relatively uniform azimuthal coverage of the stations with high SNR. The arrival times of the *P* waves are manually picked. Instrument responses are deconvolved from the seismic records, and we resample the obtained velocity records at 0.6 s interval. The Green's functions are calculated based on the method of Kikuchi & Kanamori (1991). We use the CRUST1.0 model (Laske *et al.* 2013) of the region to calculate Haskell propagator in Green's functions. The AK135 model (Kennett *et al.* 1995) is used to compute traveltimes, ray parameters and the geometrical spreading factors. We do not apply a low-pass filter to either the observed waveforms or the Green's functions, which is intended to retrieve the detailed information of slip evolution that is reflected in higher frequency components (Shimizu *et al.* 2020).

Guided by the backprojection result and the aftershock distribution (Castro *et al.* 2011b; Fig. 2), we parametrize a 2-D vertical FFM space along a strike at 310° with a total length 165 km and a width 25 km, including a total of 165 source elements

(subfaults) gridded with 5 km × 5 km spacing along both the strike and dip directions. The slip-rate function for each source element is represented by the linear B-splines at the temporal interval of 0.6 s. To test the backprojection results, we presume a maximum rupture-front speed at 5 km s^{-1} and the maximum slip-rate duration of 30 s. The earthquake can rupture at a slower speed or with a shorter duration. This parametrization is sufficiently fast to capture a high-speed rupture propagation, and long enough to flexibly represent a possible complex slip evolution that may have multiple episodes at each source element. We note that waveform fits get worse by 2.3 per cent of the variance reduction when using a slower maximum rupture-front speed of 3 km s^{-1}. The finding supports the assumption of a higher rupture speed limit in the finite-fault inversion. The total source duration is set as 30 s. For the initial rupture point, we use the relocated epicentre, 29.214°E, 113.423°W of the Canal de Ballenas earthquake (Castro *et al.* 2011b) and 12-km depth.

To evaluate the model sensitivity to the initial rupture depth, we test a set of depths at 7, 12, 17 and 22 km with the same model-domain geometry (Supporting Information Fig. S2). We find that final finite-fault slip models are insensitive to the initial rupture depth: data variance reductions differ by less than 1 per cent among these models. We also evaluate the reproducibility of the preferred model by using synthetic waveforms from the preferred model of the Canal de Ballenas earthquake (Fig. 3) to invert for a slip model. The result shows that the input model and the output model agree well (Supporting Information Fig. S3), suggesting that the finite-fault modelling of the Canal de Ballenas earthquake is robust.

2.3 Dynamic strains

To corroborate ground motion observations, we use dynamic strain records from borehole strainmeters (BSM) in the Network of the Americas (NOTA) network (Fig. 5a; see also the Data Availability section); these are four-component Gladwin-type differential capacitance strainmeters (Gladwin 1984). Raw data from these instruments come in the form of capacitance bridge counts, and we convert these to linear strains using the standard linearization expression (e.g. Barbour & Crowell 2017). For peak dynamic strains (Fig. 5), we analyse the RMS strain time-series ϵ, given by $\epsilon = \sqrt{\left[g_1^2 + g_2^2 + g_3^2 + g_4^2\right]/4}$, where g_1 is the linear strain time-series for the first gauge, and so on. Prior to calculating ϵ, we apply a two-pass Butterworth high-pass filter with a corner frequency of 0.004 Hz (250 s period) to mask out all non-seismic signals that strainmeters are sensitive to (e.g. tides, atmospheric pressure). Thus, at any given time the RMS strain is proportional to both the volume (e.g. Rayleigh waves) and shear (e.g. Love waves) strain signals in the strain wavefield.

The NOTA network has sufficient coverage to see the moveout of strain signals at epicentral distances ranging from 597 to 2460 km (Fig. 5b); these show clear arrival times of the *P* and *S* waves assuming the best-fitting source depth and the AK135 velocity model (Kennett & Engdahl 1991). We then calculate the peak value of the RMS strain time-series, $\hat{\epsilon}$ (Fig. 5c). The ratios of observed peak value to predicted peak value, from the magnitude-distance scaling relationships in Agnew & Wyatt (2014), show systematic variabilities relative to the backazimuth of the station to the best-fitting source fault plane (Fig. 5d).

2.4 Mach cone analysis

Supershear earthquakes propagate at rupture speeds exceeding the local shear wave speeds (Bouchon & Vallée 2003; Bouchon & Karabulut 2008; Bouchon *et al.* 2010) and produce abnormally large ground motions at directions away from the rupture direction, the Mach cones, which can be inferred from far-field surface wave observations (Dunham & Bhat 2008; Vallée & Dunham 2012; Bao *et al.* 2019; Hicks *et al.* 2020; Kehoe & Kiser 2020). Such earthquakes can generate far-field Mach cones and cause multiple wave fronts arriving at a receiver on the Mach cone simultaneously. Observationally, this can lead to the earthquake surface waves sharing a high resemblance with those of small earthquakes, and large amplitude ratios between the earthquakes being equal to the moment ratio (Dunham & Bhat 2008). The opening angles of the Mach cones deviate away from the rupture propagation direction and are dependent on the rupture speed and the surface wave phase velocity (Vallée & Dunham 2012).

To confirm the supershear rupture, we compare far-field Rayleigh waves from the main shock and an *M* 5 aftershock that occurred on 2009 September 13 (Fig. 2a). We obtain vertical broad-band records from available stations in the US within 30° of the main shock, a total of 665 stations. The *M* 5 aftershock shares a similar focal mechanism as the main shock, and is considered as a point source. The point-source assumption is appropriate given the magnitude difference and because we only examine teleseismic Rayleigh waves. We apply a narrow bandpass-filter to records at the 10–20 s period band for both the main shock and the aftershock. The two earthquakes are 32 km apart with a moment ratio close to 708. We cross-correlate 600 s Rayleigh waveforms of the two earthquakes for all the stations (Fig. 6). We compute the Mach cone with the rupture speed estimate as 4 km s^{-1} and the Rayleigh wave phase velocities of 3.3 and 3.95 km s^{-1} to account for possible unknown effects from the 3-D velocity structure (Ekström 2011), variation of the rupture speed during the rupture propagation and the uncertainty in the rupture speed estimation. This exercise leads to a predicted Mach cone at azimuths of 4–34° from the rupture direction towards the west coast US. The anticlockwise direction Mach cone (from north) points towards the Pacific Ocean, leaving few stations within 30° epicentral distance for the verification exercise. Therefore, we focus on the clockwise 4–34° Mach cone from the rupture direction.

2.5 Identifying dynamic triggering sites

Another aspect of the elevated ground motions is the possibility of dynamically triggered earthquakes. To investigate this in California, we apply a method that estimates probability distributions of the β-statistic by resampling earthquake catalogues (Fan *et al.* 2021). We uniformly examine seismicity within 20 km radius of 0.1° spaced grids in California. We perform the analysis in such a set-up to examine the spatial coherence and avoid missing potential triggered sites. The systematic search indicates four sites that are highly likely to have dynamically triggered earthquakes (Figs 1 and 7), including three geothermal fields. These geothermal fields were densely instrumented with seismographs at the time and seismicity rate changes can be reliably monitored.

For southern California earthquakes, we use the Quake Template Matching (QTM) catalogue (Ross *et al.* 2019) to investigate the dynamic triggering patterns. The QTM catalogue is obtained with the template matching technique and includes 1.81 million earthquakes from 2008 to 2017 (Ross *et al.* 2019). We use the '9.5dev'

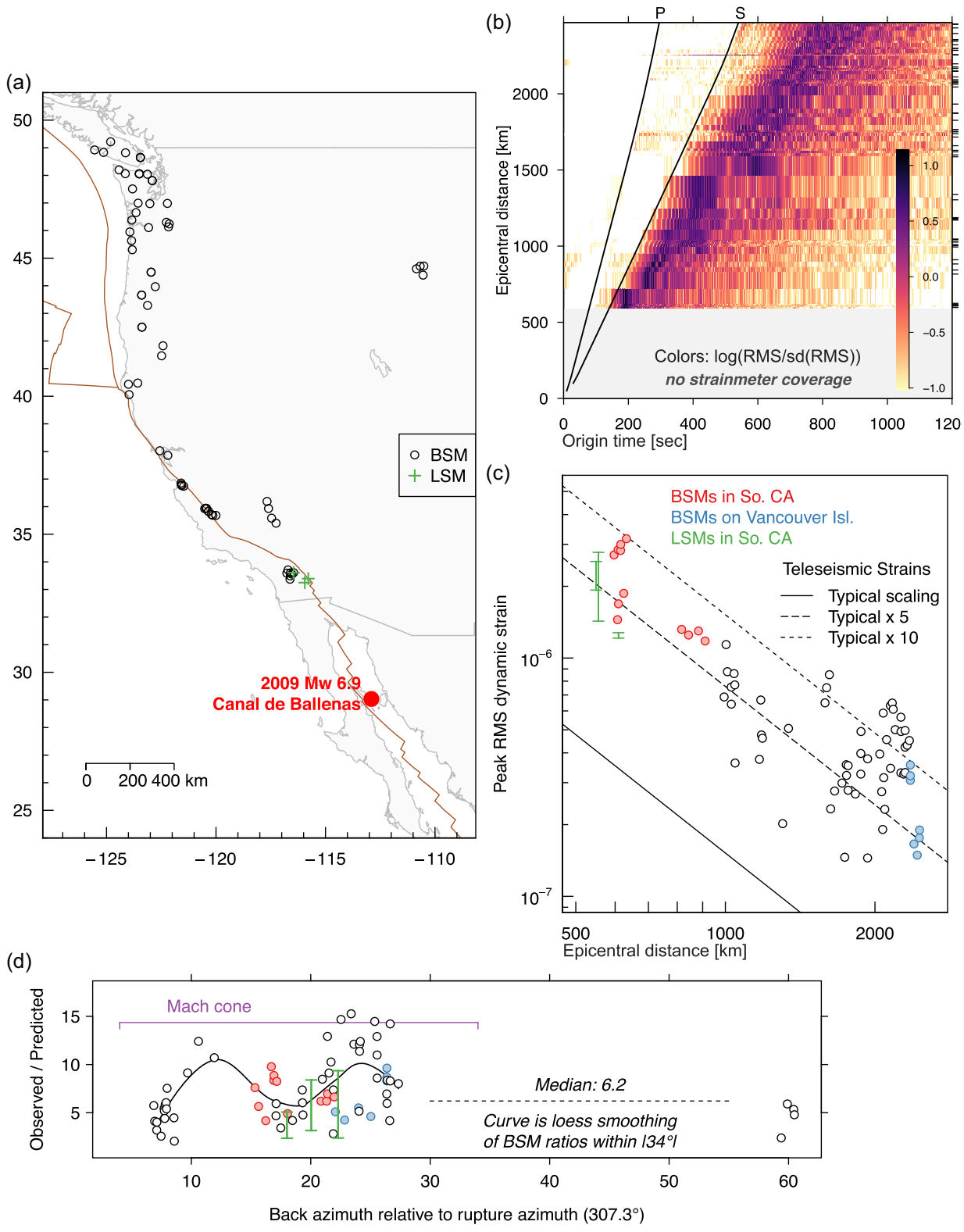

Figure 5. Dynamic strains from the 2009 M_w 6.9 Canal de Ballenas earthquake. (a) Map of strainmeter coverage including borehole strainmeters (BSM, circles), long baseline laser strainmeters (LSM, crosses) and major plate boundary faults. (b) Moveout of normalized, RMS strains calculated from high-pass filtered (4 mHz corner frequency) dynamic strain records; the normalization factor is set by the standard deviation of pre-seismic noise in each trace, and the colour scale shows the base-10 logarithm of these values. The dotted lines are traveltime curves for *P* and *S* assuming a 15 km source depth and the AK135 1-D velocity model. (c) Peak RMS strains as a function of epicentral distance along with typical magnitude-distance scaling curves for teleseismic and regional events (i.e. Agnew & Wyatt 2014). The range of values for the LSM observations represents the span of values between peak shear strain and peak areal strain. (d) Ratios of observed-to-predicted strain as a function of the backazimuth minus the best-fitting rupture azimuth.

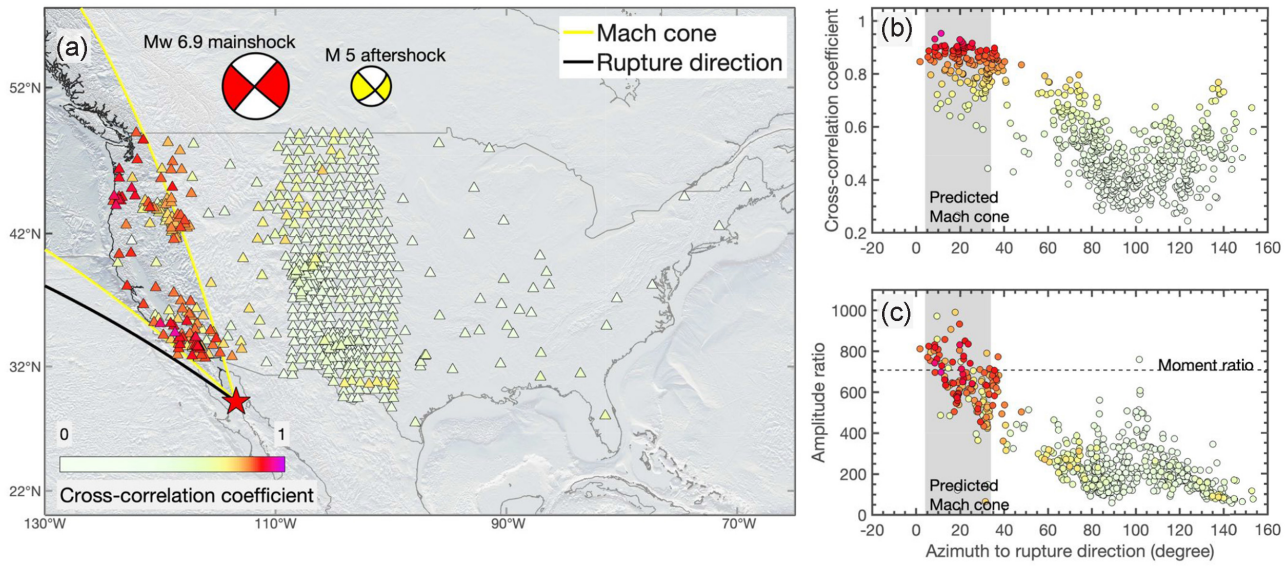

Figure 6. Rayleigh wave Mach cone analysis for the supershear rupture validation. The Mach cone is at azimuths of 4–34° relative to the rupture direction. Cross-correlation coefficients between the waveforms of the Canal de Ballenas earthquake and an M 5 aftershock (2009 September 13) are plotted in map view (a) and by azimuth relative to the rupture direction (b). (c) Rayleigh wave amplitude ratio of the two earthquakes versus azimuth relative to rupture direction.

version of the catalogue for the analysis, which has a minimum detection threshold of 9.5 times the median absolute deviation (Ross *et al.* 2019). The version of the catalogue has an approximate false detection rate of 5 per cent (Ross *et al.* 2019). For the northern California earthquakes, we use standard Northern California Earthquake Data Center Catalogue from 2007 to 2016, including 253 943 earthquakes (see Data Availability section). The Enhanced Geothermal Systems Earthquake Catalog (see Data and Resources section) is available for the Geysers area in northern California, and we use this catalogue to analyse seismicity for the region from 2007 to 2016, including 373 058 earthquakes.

Before the statistical analysis, we first evaluate the catalogues by computing the magnitude of completeness (M_c) for each grid point by using both the maximum curvature method and the goodness-of-fit test method (Wiemer & Wyss 2000; Woessner & Wiemer 2005). The two methods are applied to all the events within the spatial footprint of a given grid, and we take the M_c with the greater value as the magnitude of completeness. For the following β-statistic distribution analysis, we only analyse earthquakes of $M \geq M_c$ to assure the robustness of the identified dynamic triggering cases. The four sites in Fig. 1 have M_c as 0.5, 0.6, 0.7 and 1 for the Salton Sea Geothermal Field, Coso Geothermal Field, the Parkfield section of the San Andreas fault system and the Geysers Geothermal Field, respectively.

In triggering studies, the β-statistic (Marsan & Nalbant 2005) measures the difference between the observed number of earthquakes N_a in δt_a and the expected number Λ, a background rate, relative to the expected variability in numbers of earthquakes in that time period. Λ is the expected number of events, which is computed from $\Lambda = N_b \frac{\delta t_a}{\delta t_b}$ with N_b as the number of events during a reference time period δt_b. Accordingly, β is positive when there is an increase in seismicity rate compare to background levels, and it is negative when there is a decrease. The β-statistic is widely used, and its physical meaning is intuitive. Instead of using a fixed triggering threshold, we derive a temporally varying threshold for each candidate grid point (Fan *et al.* 2021). Our method is particularly useful for recognizing delayed triggering cases that occur after the seismic wave passage.

For a given region and time window of interest, the β-statistic distribution, Distribution-N_a, is obtained from random sampling (10 000 times) of the seismicity in a δt_a window (e.g. 2 hr) with uniformly distributed random starting time of the δt_a within 30 d before and after the P-wave arrival of the main shock (Fan *et al.* 2021). Similarly, Distribution-Λ is obtained from random sampling of the seismicity in 60 d (δt_b) with uniformly distributed random starting time within about six months of the main shock P-wave arrival (183 d before and after; Fan *et al.* 2021). From Distribution-N_a, we can obtain a triggering threshold, $\beta_{95\,\text{per cent}}$. We obtain $\beta^{\Lambda}_{5\,\text{per cent}}$ from the distribution-Λ (Fig. 7). We calculate β_0 for the seismicity rate change for a given time window and β_b of an equal-length time window immediately preceding δt_a with the same Λ. If the β_0 is greater than $\beta_{95\,\text{per cent}}$, $\beta^{\Lambda}_{5\,\text{per cent}}$ and β_b in a given region, then we interpret the candidate earthquake caused dynamically triggered seismicity during time window δt_a in that region. To further improve the robustness of this approach, we require that the catalogue (a) contains at least two earthquakes during the time window of interest for each site and (b) has at least 10 earthquakes during the reference time window.

3 RESULTS

3.1 Supershear rupture

The impetus for investigating the rupture characteristics of the 2009 Canal de Ballenas earthquake came from systematic observations of anomalous ground motions at teleseismic distances. For instance, these abnormally high ground motions caused an earthquake early warning algorithm with robust outlier suppression capabilities to trigger falsely during retrospective testing, as if a local earthquake had occurred (Cochran *et al.* 2019). As further corroboration, observations from borehole strainmeters (BSMs) from southern California to as far north as Vancouver Island show that dynamic strains are between 2.1 and 15.3 (mean 7.3) times larger than those expected for M_w 6.9 teleseisms according to the magnitude-distance scaling derived from multiple decades of recordings in southern

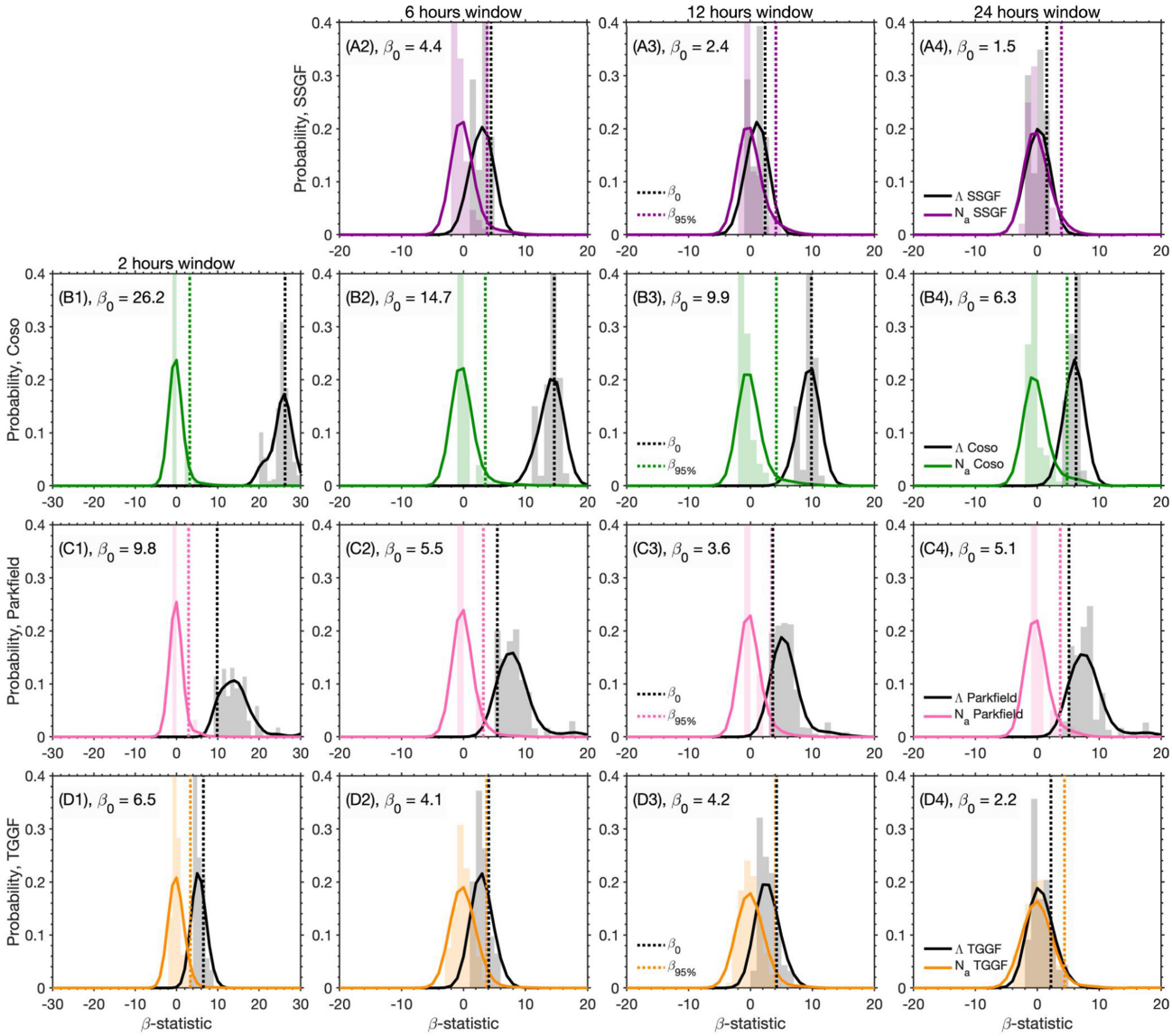

Figure 7. Dynamic triggering statistics at the Salton Sea Geothermal Field (a), Coso Geothermal Field (b), Parkfield (c) and the Geysers Geothermal Field (d). At each of these four study sides we show the β-statistic distributions of 2-, 6-, 12- and 24-hr long time windows. Distribution-N_a (coloured histogram and coloured curve) and Distribution-Λ (grey histogram and black curve) are obtained from sampling the earthquake catalogues (Fan *et al.* 2021). In each panel, the black dashed line indicates the β_0 value, showing the seismicity rate change, and the coloured solid line shows the triggering threshold $\beta_{95\,\text{per cent}}$. For example, the 2009 *M*6.9 Canal de Ballenas earthquake triggered seismicity at the Geysers Geothermal Field within 2 hr from the passing seismic waves (D1), and at the Salton Sea Geothermal Field within 6 hr (A2).

California (i.e. Agnew & Wyatt 2014, their table 1; Fig. 5); this is consistent with observations from the long-baseline strainmeters in southern California (e.g. Agnew & Wyatt 2014, their fig. 4), which are completely independent of, and more accurately calibrated than, the BSMs.

The backprojection results suggest that most of the seismic radiation (0.05–0.25 Hz band) was released along the fault segment in between the Baja California peninsula and Angel de la Guarda Island (Fig. 2a). Backprojection snapshots agree well with the fault trace, suggesting that the event ruptured ∼85 km unilaterally to the north, along its strike and stopped at the lower Delfin basin (Fig. 2b). The peak radiation intensity locates close to the M_w 6.2 aftershock, about 30 km north of the earthquake epicentre. It is unclear how the slip distributions of the two earthquakes complement each other as the backprojection images have no depth resolution for such shallow earthquakes. Due to the simple linear rupture propagation of the event, we can estimate an average rupture speed of the event by assessing the cumulative rupture distance as a function of time (inset, Fig. 2b). The total rupture lasted ∼24 s, leading to an average rupture speed of ∼4 km s^{-1} (Fig. 2b, inset). This rupture speed may have been greater than the local *S*-wave velocity (∼2.7 km s^{-1} from González-Fernández *et al.* 2005), suggesting a supershear earthquake.

The finite-fault inversion shows that the majority of slip—68 per cent of the total moment released—extended 60 km in length in the northwestern section of the model domain (Fig. 3b). The major slip patch shows an almost pure, right-lateral, strike-slip faulting style. There is another minor slip patch at the southeastern section of

the model domain (20–60 km southeast from the hypocentre), releasing 16 per cent of the total moment. For this slip patch, the focal mechanisms have dip-slip (normal fault) components (Fig. 3c), and their strike directions rotate clockwise from those seen in the major slip patch. The total moment of the Canal de Ballenas earthquake is estimated as 3.7×10^{21} N m (M_w 7.0) from the FFM. The total slip lasted for about 30 s (Fig. 4b). For the first 15 s, the rupture unilaterally propagated towards the northwest from the hypocentre (Fig. 4a), slipping a 60-km-long section of the fault with the largest slip occurring near the seafloor. The rupture speed of the high slip-rate episode is approximately 4–5 km s^{-1}. At ∼15–20 s after the earthquake initiation, the southern minor slip propagated up to 40 km away from the hypocentre (Fig. 4c). We also observe a third slip episode from 22 to 28 s that is located at ∼60–80 km northwest from the hypocentre, likely reflecting the termination of the earthquake rupture.

There is a clear Mach cone at azimuths of 4–34° (4 km s^{-1} rupture velocity and 3.3–3.95 km s^{-1} for Rayleigh wave phase velocities) relative to the rupture direction (Fig. 6), within which the possible supershear rupture of the Canal de Ballenas earthquake generated almost identical Rayleigh waves to those from the M 5 aftershock, and the surface wave amplitude ratios of the two events are close to their moment ratio (Dunham & Bhat 2008; Vallée & Dunham 2012; Bao *et al.* 2019; Hicks *et al.* 2020; Kehoe & Kiser 2020). Stations inside the predicted Mach cone have high correlation values (≥0.8), while stations outside the cone have low values (Figs 6a and b). Further, the amplitude ratios of the two earthquakes are close to 708 for stations inside the predicted Mach cone and are around 200 for stations outside the Mach cone (Fig. 6c). Incidentally, nearly all of the BSMs considered here lie within the predicted Mach cone (Fig. 5d). The distinct spatial patterns of both the cross-correlation coefficient and the observed amplitude ratios for stations in the US qualitatively confirm that the 2009 Canal de Ballenas earthquake likely ruptured at a supershear speed on average.

3.2 Teleseismic earthquake triggering

As a result of these elevated levels of dynamic strain, the Canal de Ballenas earthquake may have dynamically triggered seismicity at the Salton Sea Geothermal Field, Coso Geothermal Field, Parkfield and the Geysers Geothermal Field (Figs 1 and 7). We observe that local seismicity increased immediately (within 2 hr) at all sites except the Salton Sea Geothermal Field upon arrival of the seismic waves. Following our criteria, seismicity rate at the Salton Sea Geothermal Field for the initial 2 hr after the Canal de Ballenas earthquake was too low to be robustly analysed. The Coso Geothermal Field showed the most vigorous increase in seismicity immediately (Fig. 7b and Supporting Information Fig. S6). The elevated seismicity at the Salton Sea Geothermal Field and The Geysers Geothermal Field was less prominent than at Coso, but it lasted for about 6 hr before gradually returning to the background level (Figs 7a and c, and Supporting Information Fig. S6). At Parkfield, the triggered seismicity reached peak strength within 2 hr, gradually decreased in activity, but lasted up to 24 hr. These results are consistent with the idea that slip events can be easily triggered at regions where loading rates and/or pore pressures are high (Kilb *et al.* 2000; Gomberg *et al.* 2004; Peng *et al.* 2011). In particular, failures may have been more easily promoted at geothermal fields where high-temperature fluids are present to reduce the frictional stresses (Brodsky *et al.* 2003; Aiken & Peng 2014; Meng & Peng 2014).

4 DISCUSSION

To further understand the rupture details, we also compare the backprojection and FFMs from this study with a previous slip model obtained from space geodetic observations (Plattner *et al.* 2015; Supporting Information Fig. S2). The geodetically inferred slip-model indicates that the earthquake may have ruptured to the seafloor (Plattner *et al.* 2015), agreeing well with our FFM. In combination with the U.S. Geological Survey (USGS) earthquake location, the slip-model suggests that the earthquake may have initiated at a latitude around 29.1°, which is about 20 km south of the earthquake hypocentre that is obtained from using a few regional stations (Castro *et al.* 2011b). Given the sparse instrumentation and the high uncertainties in local velocity structure, the absolute earthquake location is challenging to constrain. Our backprojection and FFMs are insensitive to the absolute earthquake location because they are constrained by teleseismic *P* waves. Neither the backprojection nor the FFM show the southernmost slip patch seen in the geodetic slip model.

Compared to its sub-Rayleigh counterpart, supershear rupture propagation radiates shear and Rayleigh Mach waves that can generate large ground motions and dynamic stresses at much further distances (Bouchon & Vallée 2003; Dunham & Bhat 2008). Theoretically, the predicted ground motion (or amplitude ratio) would reach its maximum on the edges of the far field Mach cone (Dunham & Bhat 2008). The predicted feature deviates away from the observations that stations within the cone all recorded comparable large-amplitude ground motions (Fig. 6). The observation could have been due to a strong rupture directivity effect of a subshear rupture earthquake instead of the hypothesized supershear rupture propagation, and such subshear earthquakes have been observed in strike-slip fault systems (e.g. Gomberg *et al.* 2001; Xu *et al.* 2009). However, theoretical ground motions of Mach cone are computed from using accurate surface wave velocity and rupture speed. The observed Mach waves often share similar amplitude ratios over a range of azimuths (e.g. Bao *et al.* 2019; Hicks *et al.* 2020; Kehoe & Kiser 2020), which suggests that the 3-D velocity structure or complex rupture process may cause complex seismic wavefields.

To investigate the directivity effect hypothesis, we compute synthetic seismograms using our preferred supershear FFM (Figs 2 and 3), a subshear FFM obtained using a maximum rupture-front speed of 3 km s^{-1} (Supporting Information Fig. S3), and the GCMT point source solution. We use the Instaseis method and the PREM model to compute vertical velocity synthetic seismograms up to 5 s frequency content (Dziewonski & Anderson 1981; Driel *et al.* 2015). These synthetic seismograms are then filtered at the same 10–20 s period band which was used to evaluate the Mach waves (Fig. 8a). Further, the synthetic seismograms are filtered at 50–150 s period band to compare with the observations (Fig. 8b). The results show that amplitudes of long period (50–150 s) records can be well explained by the synthetics, while the observed short-period (10–20 s) surface waves have much larger amplitude than those of synthetic seismograms. In contrast to long-period observations (Fig. 8b), short-period Rayleigh waves in the predicted Mach cone have much larger amplitude than those outside of the Mach cone (Fig. 8a), suggesting effects of rupture propagation instead of possible high stress drop of the earthquake. The synthetic surface waves from the supershear and subshear FFMs have almost identical peak velocity amplitudes, suggesting that forward kinematic modeling without considering the 3-D velocity structure or the dynamic effects of the rupture propagation has limited resolution in distinguishing different rupture scenarios (Fig. 8a). Alternatively, the FFMs obtained from using teleseismic *P*-waves might

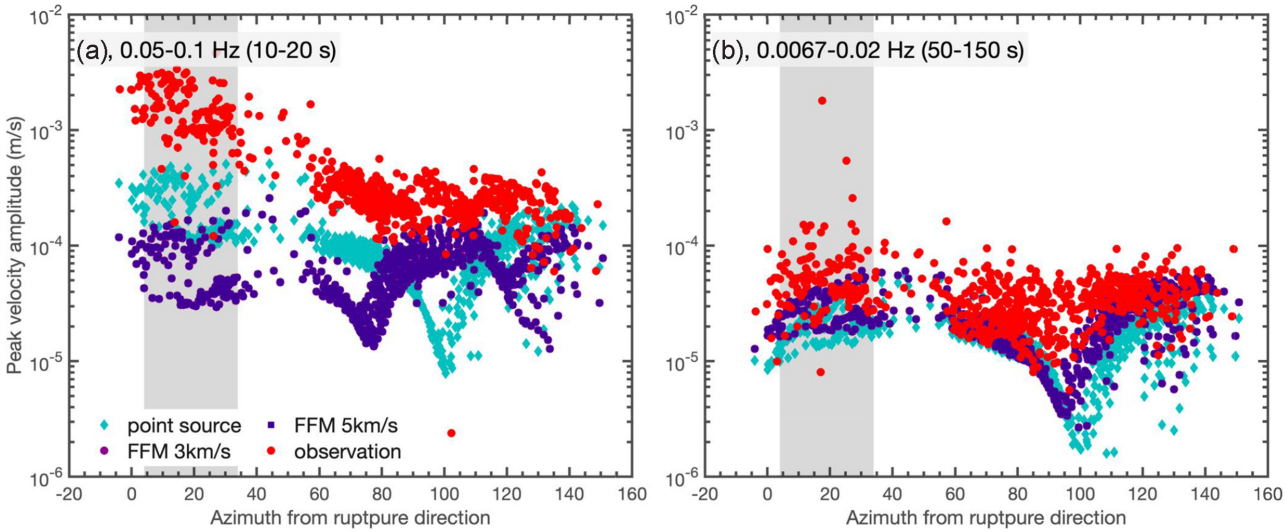

Figure 8. Observed and synthetic vertical peak ground velocities at teleseismic distances for stations in Fig. 6. (a) Peak velocity amplitudes of records filtered at 10–20 s period band. The point source synthetic data are from using the GCMT solution. The light and dark purple dots show synthetic data obtained using the preferred supershear FFM (5 km s^{-1}, Fig. 3) and the subshear FFM (3 km s^{-1}, Supporting Information Fig. S3). (b) Peak velocity amplitudes of records filtered at 50–150 s period band.

not include the source effects that are responsible for the observed high-amplitude short-period surface waves at teleseismic distance. The synthetic exercise suggests that teleseismic surface waves alone could not confirm the Canal de Ballenas earthquake rupturing at a supershear speed.

The large dynamic strain observations, backprojection image, and FFMs collectively suggest the earthquake most likely ruptured at a speed exceeding the local shear wave speed (Figs 2–6). Both dynamic rupture simulations (Andrews 1976; Aagaard *et al.* 2001; Dunham *et al.* 2003; Aagaard & Heaton 2004; Dunham & Archuleta 2004) and laboratory experiments (Rosakis *et al.* 1999) suggest that rupture speeds can become supershear when fault segments have sufficiently large initial shear stress relative to static fault strengths while the dynamic fault strengths are relatively low. It has also been shown that dynamic stresses induced by the free surface (Kaneko & Lapusta 2010), fault step overs (Hu *et al.* 2016), rough faults (Bruhat *et al.* 2016), bounded vertical extent (Weng & Ampuero 2020), and fault damage zones (Huang *et al.* 2016) can facilitate supershear rupture transition. Among these scenarios, supershear rupture in fault damage zones can propagate stably at speeds between the shear wave speed of the host rock ($V_s^{(\mathrm{host})}$) and the Eshleby speed ($\sqrt{2}V_s^{(\mathrm{host})}$), an unstable supershear speed range in homogeneous media (Burridge *et al.* 1979). Oblique slip might be another mechanism that long ruptures with both strike-slip and dip-slip components can produce steady rupture propagation at various speeds, including unstable supershear speeds (Weng & Ampuero 2020). A comparison between the observed rupture speed of the Canal de Ballenas earthquake and the local *S*-wave speed indicates that the earthquake likely propagated at an unstable supershear speed.

Our jackknife resampling test shows that the rupture velocity has an uncertainty up to ±1.4 km s^{-1} (Fig. 2, inset), in a range of 2.7–5.4 km s^{-1}. The earthquake depth and local *S*-wave velocity suffer large uncertainties. Although the USGS catalogue suggests the event occurred at a depth of 10 km (likely a default value when station coverage is poor), and the GCMT catalogue (Ekström *et al.* 2012) suggests the event depth is 12.2 km, a study using regional network shows the event ruptured at a depth of 2 km (Castro *et al.* 2011b). Local *P*-wave velocity models (Phillips 1964; González-Fernández *et al.* 2005; Lizarralde *et al.* 2007) that are obtained from active seismic surveys suggest that the *S*-wave velocity increases from ∼1.1 km s^{-1} at 0–2 km to ∼2.7 km s^{-1} at 2–8 km. The velocity models shows that the middle crust and lower crust of the region has an *S*-wave velocity of 3.2 and 3.9 km s^{-1}, respectively. The global crustal structure model (Laske *et al.* 2013) suggests that the *S*-wave velocity may vary from less than 3.5 to 3.9 km s^{-1} at depths between 3 and 12 km. Geodetic observations (Plattner *et al.* 2015) suggest that the Canal de Ballenas earthquake occurred on a fault with a locking depth of 12 km (Supporting Information Fig. S2). Our finite-fault slip model shows the majority of the slip occurred shallower than 8 km (Fig. 3b). Because of the uncertainties in both the obtained rupture speed and the local *S*-wave models, we cannot state definitively whether the Canal de Ballenas earthquake ruptured at a speed exceeding local shear wave velocity, but the strong rupture directivity and abnormally large ground motions along the west coast US support the hypothesis of a supershear rupture speed. (Fig. 5).

We observe dynamic triggering cases in California at multiple sites at two geothermal fields and Parkfield (Fig. 1). These regions were well instrumented in 2009, and may have had more complete catalogues (Schorlemmer & Woessner 2008). The San Jacinto Fault Zone in southern California, particularly the Anza region, is densely instrumented as well and its seismicity change may offer a useful reference level. However, seismicity rate changes were statistically insignificant at the San Jacinto Fault Zone to suggest dynamic triggering occurrence. Therefore, the observed non-uniform dynamic triggering distribution likely reflects the heterogeneous stress and strength conditions of the faults at that moment (Fan *et al.* 2021; Miyazawa *et al.* 2021). As we rely on sampling existing catalogues to identify dynamic triggering, we select 2 hr as the minimum time window to ensure there is a sufficient amount of earthquakes for computing the statistics (Fan *et al.* 2021). All four study sites show evidence for dynamically triggered earthquakes within 2 hr of the passing seismic waves; this was previously reported for the Salton Sea Geothermal Field (Li *et al.* 2019), but we have identified three additional cases of near-instantaneous triggering. These observations indicate that a linear failure mechanism (e.g. Coulomb stress

triggering, Kilb 2003) may have initiated the triggered earthquake sequences. However, we also observe that the sequences of triggered earthquakes lasted after the passing seismic waves, without clear main shocks (Supporting Information Fig. S4); thus, nonlinear mechanisms such as triggered creep or fluid migration (e.g. Brodsky 2006; Shelly *et al.* 2011) may represent significant factors in triggering seismicity after seismic wave passage.

5 CONCLUSIONS

The 2009 M_w 6.9 Canal de Ballenas earthquake ruptured a segment of an *en echelon* transform fault system in the Gulf of California and caused abnormally large ground motions in California. A backprojection method and a finite-fault inversion show that the earthquake rupture lasted less than 30 s and extended less than 90 km northwestwards; a minor slip episode extended up to 60 km away from the epicentre, in the southeast direction, with normal focal mechanisms. The FFM suggests that most of the slip occurred at shallow depths, with the possibility of surface (seafloor) rupture. The backprojection results suggest that the event may have predominantly ruptured towards the northwest with a fast propagation speed that likely exceeded the local shear wave speed–a supershear rupture. Further, the fast rupture speed is corroborated by a Mach cone analysis using the far-field Rayleigh waves. The earthquake caused dynamic triggering at multiple sites in California, including three geothermal fields and Parkfield. Microearthquakes at all four sites likely have been triggered near-instantaneously, but the triggering sequence duration varies from site to site.

ACKNOWLEDGMENTS

We thank the editor Dr Fukuyama, Dr Dunham, Dr Hirakawa, Dr Aagaard and an anonymous reviewer for their constructive suggestions that have led to the improvements of the paper. We thank Dr Plattner for sharing her static slip model of the Canal de Ballenas earthquake. WF acknowledges NSF grant EAR-2022441. Any use of trade, firm or product names is for descriptive purposes only and does not imply endorsement by the U.S. government.

DATA AVAILABILITY

The earthquake catalogues used in this study are from the GCMT project (Ekström *et al.* 2012), the Southern California Earthquake Data Center (QTM catalogue; Ross *et al.* 2019) and the Northern California Earthquake Data Center (NCEDC), doi:10.7932/NCEDC. The seismic data were provided by Data Management Center (DMC) of the Incorporated Research Institutions for Seismology (IRIS). The facilities of IRIS Data Services, and specifically the IRIS Data Management Center, were used for access to waveforms, related metadata and/or derived products used in this study. IRIS Data Services are funded through the Seismological Facilities for the Advancement of Geoscience and EarthScope (SAGE) Proposal of the National Science Foundation (NSF) under Cooperative Agreement EAR-1261681. Network of the Americas (NOTA) strain data were also obtained from the IRIS DMC; this material is based on services provided by the GAGE Facility, operated by UNAVCO, Inc., with support from the NSF and the National Aeronautics and Space Administration (NASA) under NSF Cooperative Agreement EAR-1724794.

REFERENCES

Aagaard, B.T. & Heaton, T.H., 2004. Near-source ground motions from simulations of sustained intersonic and supersonic fault ruptures, *Bull. seism. Soc. Am.,* **94**(6), 2064–2078.

Aagaard, B.T., Heaton, T.H. & Hall, J.F., 2001. Dynamic earthquake ruptures in the presence of lithostatic normal stresses: implications for friction models and heat production, *Bull. seism. Soc. Am.,* **91**(6), 1765–1796.

Agnew, D.C. & Wyatt, F.K., 2014. Dynamic strains at regional and teleseismic distances, *Bull. seism. Soc. Am.,* **104**(4), 1846–1859.

Aiken, C. & Peng, Z., 2014. Dynamic triggering of microearthquakes in three geothermal/volcanic regions of California, *J. geophys. Res.,* **119**(9), 6992–7009.

Ampuero, J.-P. & Dahlen, F.A., 2005. Ambiguity of the moment tensor, *Bull. seism. Soc. Am.,* **95**(2), 390–400.

Andrews, D., 1976. Rupture velocity of plane strain shear cracks, *J. geophys. Res.,* **81**(32), 5679–5687.

Atwater, T. & Stock, J., 1998. Pacific–North America plate tectonics of the Neogene southwestern United States: an update, *Int. Geol. Rev.,* **40**(5), 375–402.

Axen, G.J., Grove, M., Stockli, D., Lovera, O.M., Rothstein, D.A., Fletcher, J.M., Farley, K. & Abbott, P.L., 2000. Thermal evolution of Monte Blanco dome: low-angle normal faulting during Gulf of California rifting and late Eocene denudation of the eastern Peninsular Ranges, *Tectonics,* **19**(2), 197–212.

Bao, H., Ampuero, J.-P., Meng, L., Fielding, E.J., Liang, C., Milliner, C.W., Feng, T. & Huang, H., 2019. Early and persistent supershear rupture of the 2018 magnitude 7.5 Palu earthquake, *Nat. Geosci.,* **12**(3), 200–205.

Barbour, A.J. & Crowell, B.W., 2017. Dynamic strains for earthquake source characterization, *Seismol. Res. Lett.,* **88**(2A), 354–370.

Bouchon, M. & Karabulut, H., 2008. The aftershock signature of supershear earthquakes, *Science,* **320**(5881), 1323–1325.

Bouchon, M. & Vallée, M., 2003. Observation of long supershear rupture during the magnitude 8.1 Kunlunshan earthquake, *Science,* **301**(5634), 824–826.

Bouchon, M. *et al.*, 2010. Faulting characteristics of supershear earthquakes, *Tectonophysics,* **493**(3–4), 244–253.

Brodsky, E.E., 2006. Long-range triggered earthquakes that continue after the wave train passes, *Geophys. Res. Lett.,* **33**(15), doi:10.1029/2006GL026605.

Brodsky, E.E., Roeloffs, E., Woodcock, D., Gall, I. & Manga, M., 2003. A mechanism for sustained groundwater pressure changes induced by distant earthquakes, *J. geophys. Res.,* **108**(B8), doi:10.1029/2002JB002321.

Bruhat, L., Fang, Z. & Dunham, E.M., 2016. Rupture complexity and the supershear transition on rough faults, *J. geophys. Res.,* **121**(1), 210–224.

Burridge, R., Conn, G. & Freund, L., 1979. The stability of a rapid mode II shear crack with finite cohesive traction, *J. geophys. Res.,* **84**(B5), 2210–2222.

Castro, R.R., Perez-Vertti, A., Mendez, I., Mendoza, A. & Inzunza, L., 2011a. Location of moderate-sized earthquakes recorded by the NARS–Baja Array in the Gulf of California region between 2002 and 2006, *Pure appl. Geophys.,* **168**(8), 1279–1292.

Castro, R.R., Valdés-González, C., Shearer, P., Wong, V., Astiz, L., Vernon, F., Pérez-Vertti, A. & Mendoza, A., 2011b. The 3 August 2009 M_w 6.9 Canal de Ballenas region, Gulf of California, earthquake and its aftershocks, *Bull. seism. Soc. Am.,* **101**(3), 929–939.

Cochran, E.S., Bunn, J., Minson, S.E., Baltay, A.S., Kilb, D.L., Kodera, Y. & Hoshiba, M., 2019. Event detection performance of the PLUM earthquake early warning algorithm in Southern California, *Bull. seism. Soc. Am.,* **109**(4), 1524–1541.

DeMets, C. & Dixon, T.H., 1999. New kinematic models for Pacific–North America motion from 3 Ma to present, I: evidence for steady motion and biases in the NUVEL-1A model, *Geophys. Res. Lett.,* **26**(13), 1921–1924.

DeMets, C., Gordon, R.G., Argus, D. & Stein, S., 1990. Current plate motions, *Geophys. J. Int.,* **101**(2), 425–478.

DeMets, C., Gordon, R.G., Argus, D.F. & Stein, S., 1994. Effect of recent revisions to the geomagnetic reversal time scale on estimates of current plate motions, *Geophys. Res. Lett.,* **21**(20), 2191–2194.

Driel, M.V., Krischer, L., Stähler, S.C., Hosseini, K. & Nissen-Meyer, T., 2015. Instaseis: instant global seismograms based on a broadband waveform database, *Solid Earth,* (2), 701–717.

Dunham, E.M. & Archuleta, R.J., 2004. Evidence for a supershear transient during the 2002 Denali fault earthquake, *Bull. seism. Soc. Am.,* **94**(6B), S256–S268.

Dunham, E.M. & Bhat, H.S., 2008. Attenuation of radiated ground motion and stresses from three-dimensional supershear ruptures, *J. geophys. Res.,* **113**(B8), doi:10.1029/2007JB005182.

Dunham, E.M., Favreau, P. & Carlson, J., 2003. A supershear transition mechanism for cracks, *Science,* **299**(5612), 1557–1559.

Duputel, Z., Rivera, L., H.Kanamori & Hayes, G., 2012. W phase source inversion for moderate to large earthquakes (1990–2010), *Geophys. J. Int.,* **189**(2), 1125–1147.

Duputel, Z., Agram, P.S., Simons, M., Minson, S.E. & Beck, J.L., 2014. Accounting for prediction uncertainty when inferring subsurface fault slip, *Geophys. J. Int.,* **197**(1), 464–482.

Dziewonski, A.M. & Anderson, D.L., 1981. Preliminary reference Earth model, *Phys. Earth planet. Inter.,* **25**(4), 297–356.

Efron, B. & Tibshirani, R.J., 1994. *An Introduction to the Bootstrap,* CRC Press.

Ekström, G., 2011. A global model of Love and Rayleigh surface wave dispersion and anisotropy, 25–250 s, *Geophys. J. Int.,* **187**(3), 1668–1686.

Ekström, G., Nettles, M. & Dziewoński, A., 2012. The global CMT project 2004–2010: centroid-moment tensors for 13,017 earthquakes, *Phys. Earth planet. Inter.,* **200,** 1–9.

Fan, W. & Shearer, P.M., 2015. Detailed rupture imaging of the 25 April 2015 Nepal earthquake using teleseismic *P* waves, *Geophys. Res. Lett.,* **42**(14), 5744–5752.

Fan, W. & Shearer, P.M., 2016. Local near instantaneously dynamically triggered aftershocks of large earthquakes, *Science,* **353**(6304), 1133–1136.

Fan, W. & Shearer, P.M., 2017. Investigation of backprojection uncertainties with *M*6 earthquakes, *J. geophys. Res.,* **122**(10), 7966–7986.

Fan, W., Barbour, A.J., Cochran, E.S. & Lin, G., 2021. Characteristics of frequent dynamic triggering of microearthquakes in Southern California, *J. geophys. Res.,* **126**(1), e2020JB020,820.

British Oceanographic Data Centre, National Oceanography Centre., 2019. GEBCO_2019 Grid—a continuous terrain model of the global oceans and land, https://doi.org/10.5285/836f016a-33be-6ddc-e053-6c86abc0788e.

Gladwin, M.T., 1984. High-precision multicomponent borehole deformation monitoring, *Rev. Sci. Instrum.,* **55**(12), 2011–2016.

Goff, J.A., Bergman, E.A. & Solomon, S.C., 1987. Earthquake source mechanisms and transform fault tectonics in the Gulf of California, *J. geophys. Res.,* **92**(B10), 10 485–10 510.

Gomberg, J., Reasenberg, P., Bodin, P. & Harris, R., 2001. Earthquake triggering by seismic waves following the Landers and Hector Mine earthquakes, *Nature,* **411**(6836), 462–466.

Gomberg, J., Bodin, P., Larson, K. & Dragert, H., 2004. Earthquake nucleation by transient deformations caused by the $M = 7.9$ Denali, Alaska, earthquake, *Nature,* **427**(6975), 621–624.

González-Fernández, A., Dañobeitia, J.J., Delgado-Argote, L.A., Michaud, F., Córdoba, D. & Bartolomé, R., 2005. Mode of extension and rifting history of upper Tiburón and upper Delfín basins, northern Gulf of California, *J. geophys. Res.,* **110**(B1), doi:10.1029/2003JB002941.

Hicks, S.P. *et al.*, 2020. Back-propagating supershear rupture in the 2016 M_w 7.1 Romanche transform fault earthquake, *Nat. Geosci.,* **13**(9), 647–653.

Hu, F., Xu, J., Zhang, Z. & Chen, X., 2016. Supershear transition mechanism induced by step over geometry, *J. geophys. Res.,* **121**(12), 8738–8749.

Huang, Y., Ampuero, J.-P. & Helmberger, D.V., 2016. The potential for supershear earthquakes in damaged fault zones—theory and observations, *Earth planet. Sci. Lett.,* **433,** 109–115.

Ishii, M., Shearer, P.M., Houston, H. & Vidale, J.E., 2005. Extent, duration and speed of the 2004 Sumatra–Andaman earthquake imaged by the Hi-Net array, *Nature,* **435**(7044), 933–936.

Kaneko, Y. & Lapusta, N., 2010. Supershear transition due to a free surface in 3-D simulations of spontaneous dynamic rupture on vertical strike-slip faults, *Tectonophysics,* **493**(3–4), 272–284.

Kehoe, H. & Kiser, E., 2020. Evidence of a supershear transition across a fault stepover, *Geophys. Res. Lett.,* **47**(10), e2020GL087,400.

Kennett, B. & Engdahl, E., 1991. Traveltimes for global earthquake location and phase identification, *Geophys. J. Int.,* **105**(2), 429–465.

Kennett, B.L., Engdahl, E.R. & Buland, R., 1995. Constraints on seismic velocities in the Earth from traveltimes, *Geophys. J. Int.,* **122**(1), 108–124.

Kikuchi, M. & Kanamori, H., 1991. Inversion of complex body waves-III, *Bull. seism. Soc. Am.,* **81**(6), 2335–2350.

Kilb, D., 2003. A strong correlation between induced peak dynamic Coulomb stress change from the 1992 *M*7.3 Landers, California, earthquake and the hypocenter of the 1999 *M*7.1 Hector Mine, California, earthquake, *J. geophys. Res.,* **108**(B1), ESE 3–1-ESE 3-7.

Kilb, D., Gomberg, J. & Bodin, P., 2000. Triggering of earthquake aftershocks by dynamic stresses, *Nature,* **408**(6812), 570–574.

Laske, G., Masters, G., Ma, Z. & Pasyanos, M., 2013. Update on CRUST1.0—a 1-degree global model of Earth's crust, *Geophys. Res. Abstr.,* **15,** 2658.

Li, C., Peng, Z., Taira, T., Zhang, C., Yao, D. & Meng, X., 2019. Triggered seismicity and temporal change of seismic velocity in Salton Sea geothermal field, in *AGU Fall Meeting Abstracts,* S13D–0467.

Lizarralde, D. *et al.*, 2007. Variation in styles of rifting in the Gulf of California, *Nature,* **448**(7152), 466–469.

Lonsdale, P., 1985. A transform continental margin rich in hydrocarbons, Gulf of California, *AAPG Bull.,* **69**(7), 1160–1180.

Marsan, D. & Nalbant, S.S., 2005. Methods for measuring seismicity rate changes: a review and a study of how the M_w 7.3 Landers earthquake affected the aftershock sequence of the M_w 6.1 Joshua Tree earthquake, *Pure appl. Geophys.,* **162**(6–7), 1151–1185.

McCrory, P.A., Wilson, D.S. & Stanley, R.G., 2009. Continuing evolution of the Pacific–Juan de Fuca–North America slab window system'A trench–ridge–transform example from the Pacific Rim, *Tectonophysics,* **464**(1–4), 30–42.

Meng, L., Ampuero, J.-P., Stock, J., Duputel, Z., Luo, Y. & Tsai, V., 2012. Earthquake in a maze: compressional rupture branching during the 2012 M_w 8.6 Sumatra earthquake, *Science,* **337**(6095), 724–726.

Meng, X. & Peng, Z., 2014. Seismicity rate changes in the Salton Sea Geothermal Field and the San Jacinto Fault Zone after the 2010 M_w 7.2 El Mayor–Cucapah earthquake, *Geophys. J. Int.,* **197**(3), 1750–1762.

Miyazawa, M., Brodsky, E.E. & Guo, H., 2021. Dynamic earthquake triggering in southern California in high resolution: intensity, time decay, and regional variability, *AGU Adv.,* **2**(2), e2020AV000,309.

Nissen, E., Elliott, J., Sloan, R., Craig, T., Funning, G., Hutko, A., Parsons, B. & Wright, T., 2016. Limitations of rupture forecasting exposed by instantaneously triggered earthquake doublet, *Nat. Geosci.,* **9**(4), 330–336.

Okuwaki, R., Hirano, S., Yagi, Y. & Shimizu, K., 2020. Inchworm-like source evolution through a geometrically complex fault fueled persistent supershear rupture during the 2018 Palu Indonesia earthquake, *Earth planet. Sci. Lett.,* **547,** 116449.

Peng, Z., Wu, C. & Aiken, C., 2011. Delayed triggering of microearthquakes by multiple surface waves circling the Earth, *Geophys. Res. Lett.,* **38**(4), doi:10.1029/2002JB001937.

Persaud, P., Stock, J.M., Steckler, M.S., Martín-Barajas, A., Diebold, J.B., González-Fernández, A. & Mountain, G.S., 2003. Active deformation and shallow structure of the Wagner, Consag, and Delfin basins, northern Gulf of California, Mexico, *J. geophys. Res.,* **108**(B7), doi:10.1029/2002JB001937.

Phillips, R.P. 1964. Seismic refraction studies in Gulf of California, *Marine Geology of the Gulf of California,* 90–121.

Plattner, C., Malservisi, R., Dixon, T.H., LaFemina, P., Sella, G., Fletcher, J. & Suarez-Vidal, F., 2007. New constraints on relative motion between the Pacific Plate and Baja California microplate (Mexico) from GPS measurements, *Geophys. J. Int.,* **170**(3), 1373–1380.

Plattner, C., Malservisi, R. & Govers, R., 2009. On the plate boundary forces that drive and resist Baja California motion, *Geology,* **37**(4), 359–362.

Plattner, C. *et al.*, 2015. Space geodetic observation of the deformation cycle across the Ballenas Transform, Gulf of California, *J. geophys. Res.,* **120**(8), 5843–5862.

Ragon, T., Sladen, A. & Simons, M., 2018. Accounting for uncertain fault geometry in earthquake source inversions—I: theory and simplified application, *Geophys. J. Int.,* **214**(2), 1174–1190.

Rosakis, A., Samudrala, O. & Coker, D., 1999. Cracks faster than the shear wave speed, *Science,* **284**(5418), 1337–1340.

Ross, Z.E., Trugman, D.T., Hauksson, E. & Shearer, P.M., 2019. Searching for hidden earthquakes in Southern California, *Science,* **364**(6442), 767–771.

Rost, S. & Thomas, C., 2002. Array seismology: methods and applications, *Rev. Geophys.,* **40**(3), 2–1-2-27.

Schorlemmer, D. & Woessner, J., 2008. Probability of detecting an earthquake, *Bull. seism. Soc. Am.,* **98**(5), 2103–2117.

Shelly, D.R., Peng, Z., Hill, D.P. & Aiken, C., 2011. Triggered creep as a possible mechanism for delayed dynamic triggering of tremor and earthquakes, *Nat. Geosci.,* **4**(6), 384–388.

Shimizu, K., Yagi, Y., Okuwaki, R. & Fukahata, Y., 2020. Development of an inversion method to extract information on fault geometry from teleseismic data, *Geophys. J. Int.,* **220**(2), 1055–1065.

Sumy, D.F., Gaherty, J.B., Kim, W.-Y., Diehl, T. & Collins, J.A., 2013. The mechanisms of earthquakes and faulting in the southern Gulf of California, *Bull. seism. Soc. Am.,* **103**(1), 487–506.

U.S. Geological Survey Earthquake Hazards Program, 2017. Advanced National Seismic System (ANSS) Comprehensive Catalog of Earthquake Events and Products.

Vallée, M. & Dunham, E.M., 2012. Observation of far-field Mach waves generated by the 2001 Kokoxili supershear earthquake, *Geophys. Res. Lett.,* **39**(5), doi:10.1029/2011GL050725.

Wang, D., Mori, J. & Koketsu, K., 2016. Fast rupture propagation for large strike-slip earthquakes, *Earth planet. Sci. Lett.,* **440,** 115–126.

Weng, H. & Ampuero, J.-P., 2020. Continuum of earthquake rupture speeds enabled by oblique slip, *Nat. Geosci.,* **13**(12), 817–821.

Wiemer, S. & Wyss, M., 2000. Minimum magnitude of completeness in earthquake catalogs: examples from Alaska, the western United States, and Japan, *Bull. seism. Soc. Am.,* **90**(4), 859–869.

Woessner, J. & Wiemer, S., 2005. Assessing the quality of earthquake catalogues: estimating the magnitude of completeness and its uncertainty, *Bull. seism. Soc. Am.,* **95**(2), 684–698.

Xu, Y., Koper, K.D., Sufri, O., L.Zhu & Hutko, A.R., 2009. Rupture imaging of the M_w 7.9 12 May 2008 Wenchuan earthquake from back projection of teleseismic *P* waves, *Geochem. Geophys. Geosyst.,* **10**(4), q04006 , doi:10.1029/2008GC002335.

Yagi, Y. & Fukahata, Y., 2011. Introduction of uncertainty of Green's function into waveform inversion for seismic source processes, *Geophys. J. Int.,* **186**(2), 711–720.

Yagi, Y. & Okuwaki, R., 2015. Integrated seismic source model of the 2015 Gorkha, Nepal, earthquake, *Geophys. Res. Lett.,* **42**(15), 6229–6235.

SUPPORTING INFORMATION

Supplementary data are available at *GJI* online.

Figure S1. Backprojection resolution tests for the 2009 *M*6.9 Canal de Ballenas earthquake. (a) Theoretical resolving power (60 per cent normalized energy contours). (b) Backprojection snapshots of the theoretical resolving power. (c) Integrated backprojection image of the 2013 October 13 M_w 6.6 earthquake (60 per cent normalized energy contours). (d) Backprojection snapshots of the 2013 October 19 M_w 6.6 earthquake. Inset: stations used for backprojection. (e) Integrated backprojection image of the 2018 January 19 M_w 6.2 earthquake (60 per cent normalized energy contours). (f) Backprojection snapshots of the 2018 January 19 M_w 6.2 earthquake. Inset: stations used for backprojection.

Figure S2. Source model comparison of the 2009 *M*6.9 Canal de Ballenas earthquake. (a) A fault trace model inferred from space geodetic observations (Plattner *et al.* 2015) an the backprojection snapshots (Fig. 2b in the main text). (b) Predicted strike-slip distribution along the 120 km long and 14 km wide fault plane from geodetic observations (Plattner *et al.* 2015). Each subfault is 2 km × 2 km. The four earthquake locations are resolved from three regional stations that are distributed within 300 km (Castro *et al.* 2011a).

Figure S3. Comparison of the temporal evolution of the slip rate, projected along the model-fault strike (310°). $V_r^{\max}$ is a maximum rupture-front speed assumed in the finite-fault modelling. The dashed lines are the reference rupture speeds. The backprojection result (Fig. 2b from the main text) is overlain.

Figure S4. Cumulative seismicity and magnitude–time distributions at the four study regions (SSGF is the Salton Sea Geothermal Field; TGGF is The Geysers Geothermal Field). The *P*-wave arrival time is denoted at time 0. The top row shows the cumulative seismicity and the bottom row shows the magnitude–time distribution of the four sites.

Figure S5. Test results of different initial rupture depths for the finite-fault modelling. The cross-section of the static slip distribution for the initial rupture depth at (a) 7 km, (b) 12 km, (c) 17 km and (d) 22 km. The star shows the hypocentre and the arrow shows the rake angle (see the main text). Note that the abscissa is inverted.

Figure S6. Synthetic test for the finite-fault inversion. The cross-section of the static slip distribution for the (a) input model from the optimal FFM (Fig. 3 in the main text) and the (b) output model inverting the synthetic waveforms from the input model. The star shows the hypocentre. The arrow shows the rake angle. Note that the abscissa is inverted.

Please note: Oxford University Press is not responsible for the content or functionality of any supporting materials supplied by the authors. Any queries (other than missing material) should be directed to the corresponding author for the paper.